CHALMERS
UNIVERSITY OF TECHNOLOGY

Multiphysics simulation optimization framework for lithium-ion battery pack design for electric vehicle applications

Energy 239 (2022) 122092

Contents lists available at ScienceDirect

Energy

journal homepage: www.elsevier.com/locate/energy

Multiphysics simulation optimization framework for lithium-ion battery pack design for electric vehicle applications

Majid Astaneh [a, *], Jelena Andric [a], Lennart Löfdahl [a], Peter Stopp [b]

[a] Department of Mechanics and Maritime Sciences, Chalmers University of Technology, 412 96 Göteborg, Sweden
[b] Gamma Technologies GmbH, Danneckerstrasse 37, D-70182 Stuttgart, Germany

ARTICLE INFO

Article history:
Received 12 February 2021
Received in revised form
12 September 2021
Accepted 16 September 2021
Available online 21 September 2021

Keywords:
Lithium-ion battery
Battery pack
Multiphysics simulation
Multi-objective optimization
Electric vehicle

ABSTRACT

Large-scale commercialization of electric vehicles (EVs) seeks to develop battery systems with higher energy efficiency and improved thermal performance. Integrating simulation-based design optimization in battery development process expands the possibilities for novel design exploration. This study presents a dual-stage multiphysics simulation optimization methodology for comprehensive concept design of Lithium-ion (Li-ion) battery packs for EV applications. At the first stage, multi-objective optimization of electrochemical thermally coupled cells is performed using genetic algorithm considering the specific energy and the maximum temperature of the cells as design objectives. At the second stage, the energy efficiency and the thermal performances of each optimally designed cell are evaluated under pack operation to account for cell-to-pack interactions under realistic working scenarios. When operating at 1.5 C discharge current, the battery pack comprising optimally designed cells for which the specific energy and the maximum temperature are equally weighted delivers the highest specific energy with enhanced thermal performance. The most favorable pack design shows 8% reduction in maximum pack temperature and 16.1% reduction in module-to-module temperature variations compared to commercially available pack. The methodology for design optimization presented in this work is generic, providing valuable knowledge for future cell and pack designs that employ different chemistries and configurations.

1. Introduction

Currently, Lithium-ion (Li-ion) batteries are increasingly attracting popularity in everyday life by becoming ubiquitous in a wide variety of applications such as portable electronic devices, renewable energy systems and transportation vehicles [1,2]. The development of the economically feasible cells with high specific energies is crucial for the large-scale introduction of the electric vehicles which are of particular interest for a sustainable modern society [3]. Improvements in the performance of battery cells can be achieved either through fundamental material enhancements [4,5] or by optimally designing the already existing cells in combination with advancements in manufacturing techniques [6,7]. Xue et al. [8] argue that although the cell performance is greatly influenced by the characteristics of the occupying materials, certain cell design variables like the electrode thickness and porosity play indispensable roles to fully acquire the potential of the employed materials.

The impact of the cell engineering design on its performance has been investigated – (i) experimentally [9], (ii) using physics-based modeling frameworks [7,10,11], or recently (iii) by employing a combined approach [12]. For instance, Xu et al. [13] developed a hybrid method by combining experimental testing and physics-based modeling approaches to robustly investigate the effect of the electrode thickness on the utilization and the rate capabilities of Li-ion batteries. Typically different criteria such as specific energy, specific power, cell capacity and heat transfer efficiency have been considered to evaluate the energy efficiency and thermal performances of Li-ion battery cell designs. Becker et al. [14], highlighted the role of model-based and virtual simulation tools for speeding up the product development at lower costs. In the context of Li-ion batteries modeling, physics-based approaches such as the well-established Newman-type electrochemical model [15] provide a deep understanding about the underlying physico-chemical

* Corresponding author.
E-mail addresses: majid.astaneh@chalmers.se (M. Astaneh), jelena.andric@chalmers.se (J. Andric), lennart.lofdahl@chalmers.se (L. Löfdahl), p.stopp@gtisoft.com (P. Stopp).

https://doi.org/10.1016/j.energy.2021.122092

phenomena in a Li-ion cell sandwich and has gained enormous popularity in cell design problems [16,17]. Physics-based models are integrated recently into either design aware optimization [10,18,19] or analytical [11] frameworks to optimally determine the cell configuration. Table 1 summarizes the experimental and physics-based modeling approaches together with the employed evaluation criteria utilized recently in Li-ion cell design and performance analysis studies. The specific energy and specific power are the main objectives considered in the cell optimization studies. The thermal performance either has been analyzed in detail mainly for commercially available cells, or the research has been conducted in designing novel thermal management systems to enhance temperature uniformity within the cell [20,21]. The cell thermal performance was neither considered as a separate objective function nor was the thermal behavior of the optimally designed cells delivering maximum specific energy/power evaluated for the battery pack operation. Such studies are of utter importance bearing in mind the effects of thermal performance on both battery aging and battery pack thermal management strategies [22].

Furthermore, considering the inconsistency in the operation of the individual cells within battery pack has enormously gained popularity in recent years [22,25–27]. When battery packs are examined at the system-level, the issues such as low energy density, uncontrolled temperature rise that can potentially lead to thermal runaways, and capacity fade are observed [28]. For instance, Hosseinzadeh et al. [26] showed that the inhomogeneities in battery packs may hamper the abilities of the pack to meet the driving range targets. For these issues to be prevented, it is necessary to further understand the undesirable processes which occur at the cell level (electrodes, separator, and electrolyte). System-level simulation approach represents a powerful platform for the optimization of cell architecture, operational strategies, and life duration by striking the balance between the energy efficiency and the aforesaid unwanted issues [29].

The electrical models of Li-ion cells have been broadly integrated into the system-level modeling framework of the battery packs due to their straightforward implementation and computational efficiency [25,27,30]. The electrochemical models, on the other hand, have attracted attention recently due to their ability to improve the accuracy and predictability in multiphysics modeling of the battery packs and electric vehicles [17,22,26,31]. For example, Liang et al. [32] proposed a novel thermal management strategy for a Li-ion battery module by developing a multi-electrochemical-thermal modeling framework. The model was capable to capture the dynamic evolutions of local current density and Li concentration for detailed electrochemical analysis. Gao et al. [2] incorporated a control-oriented electrochemical-thermal model of Li-ion batteries into electric vehicle battery management system. Furthermore, the electrochemical models make it possible to access cell design variables and material properties which are crucial when modeling the interactions between the cell structure and the pack performance. The studies focusing on battery packs have so far aimed at either quantifying the pack performance by highlighting cell-to-cell variations or controlling the pack operation by considering the commercially available cells [33,34]. Investigating the interactions between the cell level and the pack level in the early design stage of the cell is scarce in the literature. Campbell et al. [7] developed an integrated multi-scale framework to optimally find the number of layers of Li-ion pouch cells to maximize the useable energy while addressing the fast charging and specific acceleration issues of plug-in hybrid electric vehicles (PHEVs) and battery electric vehicles (BEVs). Their methodology employed a top-down approach from the vehicle powertrain level to the cell electrode level. Nevertheless, the study did not address the impact of the cell-to-cell extrinsic variations originating from the pack electrical topology on its performance. Up to date, the performance of the optimally designed cells operating jointly in battery modules and packs has remained questionable. During realistic operating scenarios, the current flows unequally among different branches and leads to temperature gradients across the pack which can negatively affect the thermal performance and the deliverable energy of the pack. Non of the previous works have clearly quantified the battery pack performance composed of differently designed cells.

The present work fills the afore-stated knowledge gaps by employing the multiphysics simulation framework previously developed by the authors [31] to perform the optimization studies for improved pack design. The study focuses on the assessment of the cell-to-pack interactions for the purpose of optimal pack design. For specific performance objectives chosen at the pack level, the cell architecture (cell design parameters) is adjusted and consequently used to generate a novel modular Li-ion battery pack for vehicle applications. The proposed multi-physics simulation and multi-criteria design optimization framework aims at providing energy- and thermal-conscious guidelines for cell and pack manufacturers already at the initial design stage. The simulations and optimizations are conducted in GT-AutoLion/GT-SUITE, a leading software for multiphysics system simulations [35].

2. Methodology

First the mathematical modeling approach and the applied parameter identification technique are encapsulated succinctly in Subsection 2.1. The cell design optimization and the pack performance analysis are then presented in detail in Subsections 3.1 and 3.2, respectively. In the end, Subsection 2.4 recapitulates the proposed multiphysics simulation and systematic analysis framework.

2.1. Model development and parameter identification

In the previously published work by the authors [31], a model parametrization framework for the Li-ion battery cell and pack based on the calibration optimization methodology has been

Table 1
Literature review of cell design and performance evaluation.

Reference	Experimental	Modeling	Performance Evaluation Criteria				Methodology
			Specific Energy	Specific Power	Cell Capacity	Heat Transfer	
[9]	✓		✓				Testing and analysis
[12,13]	✓	✓	✓	✓			Testing, modeling and analysis
[23,24]	✓	✓				✓	Testing, modeling and analysis
[11]		✓	✓	✓			Analysis of variance
[8,10]		✓	✓				Single objective optimization
[19]		✓	✓	✓			Single objective optimization
[18]		✓	✓	✓	✓		Multi-objective optimization

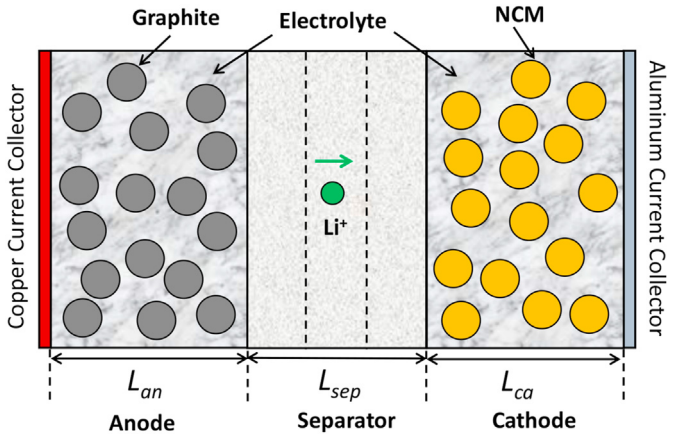

Fig. 1. The representative cell structure used for thermally coupled P2D electrochemical model.

proposed for the electric vehicle applications. A thermally enhanced Newman type pseudo two-dimensional (P2D) cell electrochemical model [15] was integrated into the module-to-module descritized pack electrical model [25,31] to consider cell-to-cell variations in inhomogeneous large traction battery packs. Fig. 1 illustrates the cell structure consisting several layers including current collectors, porous electrodes and the separator along the cell thickness.

Table 2 summarizes the governing equations together with the boundary conditions at each domain for the cell thermally coupled P2D electrochemical model [11,31,36]. The model computes solid and electrolyte phase Li concentration (c_s and c_e), potential in both the solid (φ_s) and the electrolyte (φ_e), intercalation current density (j^{Li}), as well as cell temperature (T) by solving for mass, charge and energy conservation along with electrochemical kinetics.

The battery cell/pack modeling and calibration optimization technique were implemented in the GT-SUITE/GT-AutoLion, a leading multiphysics system level simulation software [35]. Readers are referred to the authors' previous work [31] to obtain detailed information about the model development and the employed parameter identification approach. The cells/pack dynamic responses (voltage and temperature) were validated using the experimental data provided by NorthVolt AB [37] for the commercially available cylindrical cells made of graphite and NMC as the anode and the cathode active materials, respectively. Fig. 2 compares the simulated cell voltage and temperature with the experimental observations for four cell samples used during the model calibration stage. The tests were preformed for three consecutive cycles including in between periods of rest. A dual stage charging strategy with C-rate of 1/3 followed by constant voltage step was employed for all cycles while C-rates of 1/5, 1/2 and 1 were considered for the first, second and third cycles, respectively. The relative root mean square error (RRMSE) for the voltage and temperature predictions are 1.08% and 3.07%, respectively. It is worth noting that the C-rate is a measure of the rate at which a battery is being charged or discharged and it is defined as the ratio of the charge/discharge current ($I_{c/d}$) with respect to cell nominal capacity (C_{nom}). Therefore the applied charge/discharge

Table 2
Governing equations together with boundary conditions for the cell P2D electrochemical-thermal model.

Description	Governing equations and boundary conditions	Eq.
Solid phase: conservation of Li^+	$\frac{\partial c_s}{\partial t} = \frac{D_s}{r^2}\frac{\partial}{\partial r}\left(r^2\frac{\partial c_s}{\partial r}\right)$; $\frac{\partial c_s}{\partial r}\|_{r=0} = 0, -D_s\frac{\partial c_s}{\partial r}\Big\|_{r=R_s} = \frac{j^{Li}}{a_s F}$.	(1)
Electrolyte phase: conservation of Li^+	$\frac{\partial(c_e\epsilon_e)}{\partial t} = \frac{\partial}{\partial x}\left(D_e^{eff}\frac{\partial c_e}{\partial x}\right) + \frac{1-t_+^0}{F}j^{Li}$; $\frac{\partial c_e}{\partial x}\|_{x=0} = \frac{\partial c_e}{\partial x}\Big\|_{x=L_{an}+L_{sep}+L_{ca}} = 0$.	(2)
Solid phase: charge conservation	$\frac{\partial}{\partial x}\left(\sigma^{eff}\frac{\partial\varphi_s}{\partial x}\right) = j^{Li}$; $-\sigma^{eff}\frac{\partial\varphi_s}{\partial x}\|_{x=0} = -\sigma^{eff}\frac{\partial\varphi_s}{\partial x}\Big\|_{x=L_{an}+L_{sep}+L_{ca}} = \frac{I}{A}$, $\frac{\partial\varphi_s}{\partial x}\|_{x=L_{an}} = \frac{\partial\varphi_s}{\partial x}\Big\|_{x=L_{an}+L_{sep}} = 0$.	(3)
Electrolyte phase: charge conservation	$\frac{\partial}{\partial x}\left(k^{eff}\frac{\partial\varphi_e}{\partial x}\right) + \frac{\partial}{\partial x}\left(k_D^{eff}\frac{\partial(\ln c_e)}{\partial x}\right) + j^{Li} = 0$; $\frac{\partial\varphi_e}{\partial x}\|_{x=0} = \frac{\partial\varphi_e}{\partial x}\Big\|_{x=L_{an}+L_{sep}+L_{ca}} = 0$.	(4)
Electrochemical kinetics	$j^{Li} = a_s i_0\left[exp\left(\frac{\alpha_{an}F}{RT}\eta\right) - exp\left(\frac{\alpha_{ca}F}{RT}\eta\right)\right]$	(5)
Overpotential	$\eta = \varphi_s - \varphi_e - U$.	(6)
Effective properties	$\psi_e^{eff} = \psi_e\epsilon_e^{1.5}$, $\psi_e = D_e$ and k.	(7)
Voltage	$V = \varphi_s(x = L_{cell}) - \varphi_s(x = 0) - \frac{R_c}{A}I$.	(8)
Reaction surface area	$a_s = \frac{3\times(1-\epsilon_e-\epsilon_f)}{R_s}$.	(9)
Energy conservation	$\frac{d(C_pT)}{dt} = -hA_{cell}(T - T_{amb}) + Q_{gen}$.	(10)
Heat generation	$Q_{gen} = (U - V)I - IT\frac{dU}{dT}$.	(11)

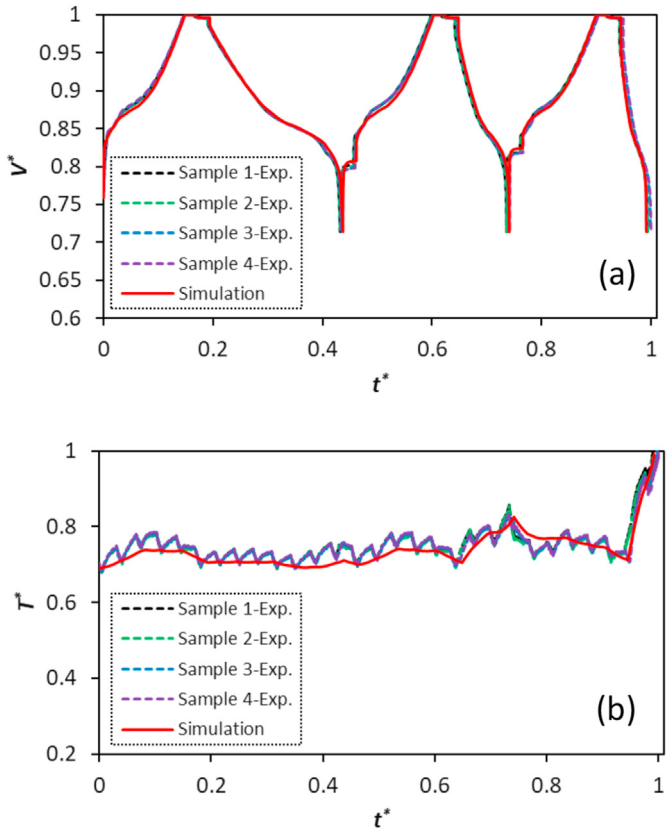

Fig. 2. P2D electrochemical-thermal model validation. **(a):** Cell voltage profile. **(b):** Cell temperature profile.

current can be obtained as:

$$I_{c/d} = C_{rate} C_{nom}. \tag{12}$$

In this work, the material properties and the design parameters of the fully characterized battery cell model are considered as the starting point in the optimization procedure, hereafter referred to as the *baseline design* properties.

2.2. Cell design optimization

This subsection describes the selection of the design factors (Subsection 2.2.1) together with the objective function definition and the optimization constraints (Subsection 2.2.2).

2.2.1. Design factors selection

The literature review shows that battery cell performance can be optimized by manipulating a diverse set of parameters and employing a suitable algorithm. For instance, Xue et al. [8] developed a sophisticated optimization framework to maximize cell specific energy while considering a large number of parameters representing cell morphology and material transport properties. Other authors [10,16] have proposed more straightforward approaches based on one- or two-parameter optimization methodologies to configure the electrode engineering design by altering the thickness and porosity of positive electrode. The literature survey also points out that the electrode thickness, porosity and particle size are key design variables for the performance optimization of Li-ion batteries [11,18,38].

Variations in thickness and porosity of the cell electrodes lead to trade-offs in cell balancing (i.e. operational capacity) and cell cycling performance (i.e. voltage response). As seen from Table 2, the electrodes' porosities and thicknesses implicitly influence the cell voltage and temperature. Moreover, the electrodes' capacities (C_{an} and C_{ca}) are correlated to the afore-stated design factors as [36]:

$$C_{an} = (1 - \epsilon_{e,an} - \epsilon_{f,an}) F L_{an} A_{an} c_{s,an,max} |x_{100\%} - x_{0\%}|, \tag{13}$$

$$C_{ca} = (1 - \epsilon_{e,ca} - \epsilon_{f,ca}) F L_{ca} A_{ca} c_{s,ca,max} |y_{100\%} - y_{0\%}|, \tag{14}$$

Where ϵ_e is the electrolyte volume fraction (i.e. the electrode's porosity), ϵ_f is the filler volume fraction, F is the Faraday's constant, L is the electrode thickness, A is the electrode surface area, $c_{s,max}$ is the maximum solid phase concentration, and x and y are the stoichiometry factors of the anode and cathode, respectively.

Increasing electrode thickness increases the internal resistance of the cell, which results in a higher potential drops across the electrode. Thicker electrodes provide higher volumes of active materials resulting in higher discharge capacities [8,18]. Moreover, even though higher electrode porosity facilitates the Li-ion transport in the electrolyte phase, it leaves the electrode compartment with less active material and thus negatively affects the deliverable specific energy [18]. Particle size influences the diffusion time and the surface area of the active material occupying the porous electrodes [39,40]. However, including the particle size into the cell design optimization without considering the solvent reduction and aging phenomena typically results in the smallest defined particle size as an optimal solution [8,19]. Reducing the particle size increases the intercalation rate and decreases the kinetic resistance hence maximizing the cell specific energy [11]. Including particle size in the optimal cell design is thus purposeful when accounting for the aging effects [10,18].

The present optimization study considers the thickness and porosity of both electrodes (anode and cathode) to be the major design parameters affecting the performance of healthy Li-ion battery cells.

2.2.2. Objective function and constraints

Maximizing specific energy (energy per unit mass) and specific power (power per unit mass) has been broadly used in design optimization of Li-ion battery cells [10,11,18,19]. Cell-to-cell variations in battery packs with a large number of cells connected in series and parallel lead to imbalanced current flows causing uneven temperature distribution. Temperature differences across the battery pack can substantially reduce the amount of energy delivered by the pack due to a rapid temperature rise in heavily loaded cells [26,27]. Therefore, it is utterly important to predict the eventual increase in battery cell temperatures under cycling, during the initial design phase. For that reason, the present study considers the weighted sum approach [41], to build the composite objective function F_{cell} made of the specific energy and the maximum temperature experienced by the cell under cycling. The multi-objective optimization maximizes F_{cell} as:

$$Maximize: \; F_{cell}(x_i) = w_E . \left(\frac{E_{cell}(x_i)}{E^b_{cell}(x_{i,b})} \right) - w_T . \left(\frac{T_{max,cell}(x_i)}{T^b_{max,cell}(x_{i,b})} \right), \tag{15}$$

where E_{cell} is the cell specific energy, $x_i \, (i = [1:4])$ represents one of the four design factors including thickness and porosity of both electrodes (see Subsection 2.2.1), w_E and w_T are the weight factors for the specific energy and temperature, respectively, and the superscript b represents the corresponding baseline parameter values which are considered for the purpose of the normalization to fairly

construct the composite objective function from the constituent sub-objectives. Furthermore, $T_{\max,cell}$ represents the maximum cell temperature during the discharge process obtained by coupling the lumped energy conservation equation with the cell electrochemical model to account for the cell temperature evolution over time [31,36].

The specific energy is calculated by the integration of the delivered instantaneous power of the cell over discharge time [10,11]:

$$E_{cell} = \frac{1}{M_{cell}} \int_0^{t_{d,cell}} V_{cell}(t) I_{d,cell} dt, \tag{16}$$

where M_{cell} is the total mass of the cell, $t_{d,cell}$ is the end of discharge time, V_{cell} is the cell voltage response obtained from the P2D electrochemical model [11,31], and $I_{d,cell}$ represents the applied electric current for the cell.

The aforeformulated cell design optimization problem is subjected to several constraints and assumptions as follows:

- The dimensions of the cell outer enclosure are the same as for the cell baseline design.
- The anode-to-cathode capacity ratio (a/c) is kept within the range $1.1 \leqslant a/c \leqslant 1.4$ to minimize the susceptibility of Li deposition under cell cycling [9,16].
- The discharge current of 1.5 C (relative to the cell baseline design) has been considered as the most severe case scenario for the electric mining vehicle application under consideration [31] and is therefore used as the cell operational current for evaluating different design cases in the optimization process.
- The final discharge time of the cell corresponds to the time cell reaching lower cut-off voltage threshold recommended by the manufacturer.

2.3. Pack performance analysis

Modeling and predicting the operation and performance of battery packs have been oversimplified for many years and the issue has drawn outstanding attention recently [22,42,43]. Multiple factors can impose inconsistencies on the operation of the individual cells and modules which are electrically connected in series and parallel to fulfill the demanded voltage and capacity of large battery packs [44]. The ratio of the interconnection resistance to cell resistance has been considered as one the parameters that gives rise to an unequal current distribution and hence temperature gradients between parallel branches [27]. A sudden rise in temperature or a rapid drop of potential in highly load branches leads to underutilization of the energy available in battery packs which in turn hinders the driving range of the battery-powered vehicles [26]. The degree of inhomogeneity can be further amplified under pack long-term operation due to rapid degradation of the cells subjected to severe operational conditions in terms of aging stress factors [22].

Therefore, the thermally coupled electrochemical model of the cell and the electrical model of the pack are in the present study consolidated in a comprehensive multiphysics model to systematically evaluate the performance of the optimally designed cell while taking into account the electrical topology of the pack.

Furthermore, to consider the impact of imbalanced current distributions, the battery pack is discretized into multiple modules connected in parallel. Fig. 3 provides a generic schematic representation of the battery pack model comprising N parallel branches

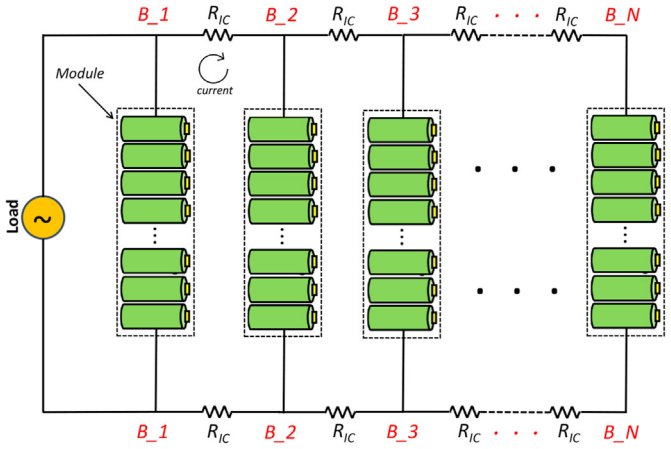

Fig. 3. A schematic representation of the module-to-module discretized battery pack.

$B_1 - B_N$. Each branch represents one lumped module consisting of serially connected cells. The total number of cells and modules considered herein corresponds to commercially available Northvolt Li-ion battery pack considered in the authors' previous work [31].

The operational performance of the pack is assessed by considering pack-level specific energy E_{pack} defined as:

$$E_{pack} = \frac{1}{M_{cell} n_{cell,se} n_{cell,pa}} \int_0^{t_{d,pack}} V_{T,pack}(t) I_{d,pack} dt, \tag{17}$$

where $n_{cell,s}$ and $n_{cell,p}$ are the number of cells connected in serial and parallel, respectively, $V_{T,pack}$ is the pack terminal voltage, $I_{d,pack}$ is the applied discharge current and $t_{d,pack}$ is the pack discharge time.

In addition, the state of charge (SOC) links directly to the vehicle driving range providing the information about the ratio of the remaining capacity of the battery pack to its present maximum capacity [45,46]:

$$SOC_{pack}(t) = SOC_{pack}(0) - \frac{\int_0^t I_{d,pack} dt}{n_{cell,pa} C_{0,cell}}, \tag{18}$$

where $SOC_{pack}(0)$ is the initial state of charge, t is the time of discharge and $C_{0,cell}$ is the operational capacity of the cell obtained from the low rate capacity identification [35]. Therefore, the SOC at the end of discharge indicates how much of the available capacity of the battery system has been left unused.

Liu et al. [22] have suggested the average standard deviation as a measure of the degree of inconsistency in the operation of parallelly connected cells in battery packs. In this work, the average standard deviation of the temperature is considered along with the maximum temperature of the pack to demonstrate the thermal performance of the optimally designed cell under pack operation. Here, the standard deviation of the temperature σ_T at the time instance t is defined as [47]:

$$\sigma_T(t) = \sqrt{\frac{1}{N-1} \sum_{j=1}^{N} \left(T_j(t) - \mu_T(t)\right)^2}, \tag{19}$$

where N is the number of the modules connected in parallel within the pack, T_j is the temperature of the jth module, and μ_T is the mean value of the temperature, i.e.,

$$\mu_T(t) = \frac{1}{N}\sum_{j=1}^{N} T_j(t). \tag{20}$$

Thereby, the average standard deviation of the temperature within the pack is obtained as:

$$\sigma_{T,avg} = \frac{1}{t_{d,pack}} \int_0^{t_{d,pack}} \sigma_T(t)dt. \tag{21}$$

The battery pack simulations were carried out under the following assumptions:

- The pack arrangement is the corresponding baseline commercially available pack configuration. This choice is made for the purpose of the pack-level performance assessment using the optimally designed cell.
- No intrinsic cell-to-cell variations arising from the manufacturing process have been considered in the pack model.
- The inhomogeneity in the operation of the individual cells has been imposed extrinsically by considering the interconnection resistances between the parallel branches. The interconnection resistance is assumed to be 10% of the cell nominal internal resistance at 50% SOC and the ambient temperature 25 °C [25,26]. The interconnection resistance leads to imbalanced current flows among parallel branches which in turn results in uneven temperature profiles in highly parallelized battery packs [26].
- Here the focus is on the influence of the pack electrical topology and therefore current imbalances on the temperature gradient within the pack (i.e. variations in module-to-module heat generation rates). The variations in heat dissipation rates due to cooling effects have not been considered in this work. In other words, all cells are assumed to be subjected to the same thermal boundary conditions. This assumption has been made since the selected design variables are cell design factors (e.g. the thicknesses of the electrodes and their porosities) not the cooling circuit design and operation parameters. The afore-stated parameters together with the imposed current imbalances (due to the electrical positioning of the cells within the pack) contribute to the heat generation rates. For more accurate predictions of the temperature distributions, the heat rejection rates from the cells to the coolant should be captured by detailed thermal modeling of the cooling circuit and subsequently coupled with the developed pack electrical model (see for example Ref. [48]).
- The battery pack performance is evaluated under constant discharging currents of 1.5 C and C/2.
- The pack is considered fully discharged when either the pack terminal voltage reaches the lower cut-off voltage threshold or the maximum temperature within the pack exceeds the highest allowable value recommended by the pack designer. Under battery pack operation, the individual cells/modules may experience different working conditions due to the variations in either cell manufacturing process or battery pack electrical-thermal design. To avoid some unwanted problems like thermal runaway propagation and accelerated aging, the local temperatures within the pack are measured and a cut-off temperature limit is set to stop the pack operation and thus prevent the afore-stated phenomena to occur.

2.4. Multiphysics simulation and systematic analysis framework

Multiphysics electrochemical-thermally and electrically coupled model of battery packs is essential to capture the underlying phenomena that occur when vehicles operate in real world [29]. GT-AutoLion software [35] efficiently and robustly integrates such models into GT-SUITE system-level modeling and optimization framework. In addition, the software provides an accurate database for battery material properties over a wide range of conditions [31,49].

Fig. 4 graphically summarizes the comprehensive modeling framework developed herein and integrated in GT-Autolion/GT-SUITE. Multiphysics simulations were carried out to determine optimal design of cells by the systematic analysis of their joint performance under battery pack operations. This approach provides reliable guidelines to cell manufacturers by bringing forth valuable inputs about the interaction between the cell and pack levels already at the cell design phase.

3. Results and discussion

This section elaborates the cell design optimization (Subsection 3.1) and the corresponding pack performance (Subsection 3.2) providing a comprehensive analysis of the cell-pack interactions based on the developed multiphysics simulation framework (Subsection 3.3). The simulation results are shown in their dimensionless form:

$$x^*_{cell} = \frac{x_{cell}}{x^b_{cell}}, \quad E^* = \frac{E}{E^b_{cell}(at\ I_{d,cell} = 1.5\ C)}, \quad T^*_{max} = \frac{T_{max}}{T^{cut-off}_{max}},$$
$$C^*_{cell} = \frac{C_{cell}}{C^b_{0,cell}}, \quad V^*_{cell} = \frac{V_{cell}}{V^{cut-off}_{cell,max}}, \quad t^*_{pack} = \frac{t_{pack}}{t^b_{d,pack}(at\ I_{d,pack} = 1.5\ C)}, \tag{22}$$

where the superscript * represents the dimensionless quantities and the superscript b stands for the baseline values of the commercially available battery cell/pack. Cell design factors are denoted by x, E is the cell/pack specific energy, $T_{\max}$ is the maximum cell/pack temperature during the discharge process, C_{cell} and V_{cell} are the delivered cell capacity and voltage, respectively, and t_{pack} is the discharge time of the pack. Note that $T_{\max}$ is normalized using the maximum cut-off temperature for the pack $T^{cut-off}_{max}$, C_{cell} with the operational capacity of the baseline cell at C/20 ($C^b_{0,cell}$), V_{cell} with the cell cut-off voltage $V^{cut-off}_{cell,max}$ and t_{pack} by using the discharge time of the baseline pack at 1.5 C discharge rate ($t^b_{d,pack}$).

3.1. Cell design optimization

Four design factors are considered in this study for the purpose of cell design optimization comprising anode thickness L_{an}, cathode thickness L_{ca}, anode porosity ϵ^*_{an} and cathode porosity ϵ^*_{ca}. Table 3 specifies the ranges of the design factors which were chosen based on the values previously used in several studies for similar purposes [8,19].

Four optimization cases are defined to alter the contributions of the specific energy and the maximum cell temperature in the multi-objective design optimization problem formulated by Equation (15). Case A only considers the specific energy as the objective function. The contribution of the specific energy in the composite objective function for cases B and D are three times and one third of the maximum cell temperature, respectively. In case C, both the

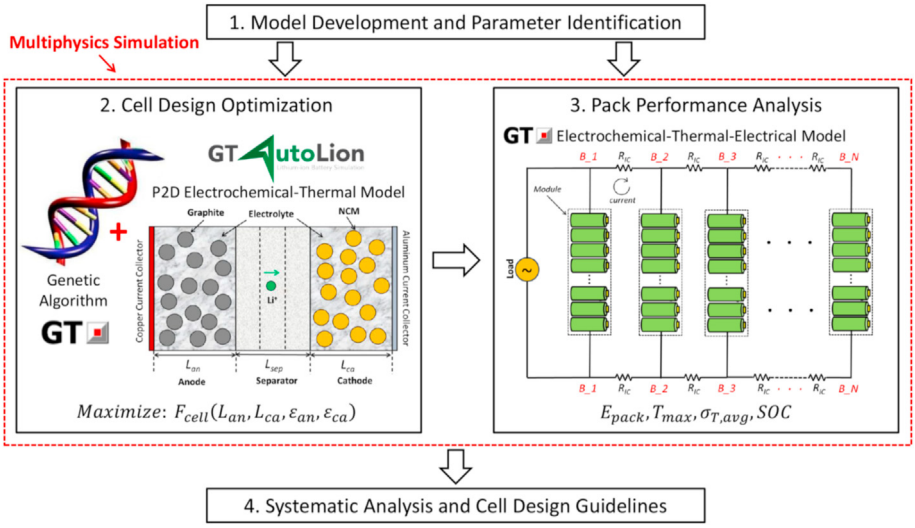

Fig. 4. Multiphysics simulation and systematic analysis framework for designing Li-ion cells.

Table 3
Lower and upper bounds of the dimensionless design factors used for the cell design optimization.

Design Factor	Lower Bound	Upper Bound
L^*_{an}	0.49	3.09
L^*_{ca}	0.52	3.23
ϵ^*_{an}	0.43	2.61
ϵ^*_{ca}	0.56	3.33

specific energy and the maximum cell temperature contribute equally to finding the cell optimal design.

- Case A: $\frac{w_E}{w_E+w_T} = 1$; $\frac{w_T}{w_E+w_T} = 0$.
- Case B: $\frac{w_E}{w_E+w_T} = 0.75$; $\frac{w_T}{w_E+w_T} = 0.25$.
- Case C: $\frac{w_E}{w_E+w_T} = 0.5$; $\frac{w_T}{w_E+w_T} = 0.5$.
- Case D: $\frac{w_E}{w_E+w_T} = 0.25$; $\frac{w_T}{w_E+w_T} = 0.75$.

The optimal values of the dimensionless design factors together with the resulting specific energy and the maximum cell temperature for all optimization cases and the baseline cell at 1.5 C discharge current are summarized in Table 4.

For case A, where only the specific energy is considered as the objective function, 20% thicker and 50% less porous electrodes compared to the baseline case are found to increase the cell capacity and hence the delivered energy by 13%. When the maximum cell temperature is included in the composite objective function (case B, maximum cell temperature weight factor 0.25), the optimal values for the electrode thicknesses (both cathode and anode) are nearly the same as in the baseline case. For cases C and D where the maximum cell temperature is considered with weight factors 0.5 and 0.75, respectively, the optimal values for the electrode thicknesses are 40–50% lower compared to the baseline case to reduce the cell internal resistance and therefore limit the temperature rise during discharge. Moreover, it is found that the optimal electrode porosities are smaller than the baseline value for all four cases. Cases A, B and C yield 44–52% less porous electrodes than the baseline case, while case D gives 17% less porous anode and similar cathode porosity compared to the baseline case. These results demonstrate that the electrodes with lower porosities than the baseline values maximize cell specific energies due to the increased volumes of the occupying active materials even though these increased volumes contribute to ion transport limitations. Moreover, it should be mentioned that the maximum cell temperature remains below the cut-off value for all cases. The optimally designed cell in case A has the thickest and the least porous electrodes for holding more active materials to increase the cell discharged capacity and maximize the drawn specific energy. Consequently, the cell experiences higher internal resistance leading to 18.8% higher maximum temperature than the baseline case. Moreover, the maximum temperature corresponds to 95% of the cut-off temperature threshold for the battery pack. Conversely, the optimally designed cell in case D has 10% lower specific energy in comparison with the baseline scenario, resulting in 16.3% reduction in the maximum cell temperature, which corresponds to 67% of the pack threshold temperature. This has been achieved by minimizing the thicknesses of both electrodes and keeping the porosities close to the baseline case. The optimally designed cell in case B leads to 12% improvement in the specific energy at the cost of 8.8% increase in the maximum temperature compared to the baseline case with the electrodes as thick as the baseline case and 50% lower porosities. The specific energy and the maximum

Table 4
Cell design optimization results at 1.5 C discharge current.

Design Factor	Baseline Case	Optimization Cases			
		Case A	Case B	Case C	Case D
L^*_{an}	1.0	1.16	0.97	0.61	0.49
L^*_{ca}	1.0	1.21	1.01	0.65	0.52
ϵ^*_{an}	1.0	0.48	0.52	0.48	0.83
ϵ^*_{ca}	1.0	0.56	0.56	0.56	1.0
Evaluation Index					
E^*_{cell}	1.0	1.13	1.12	1.05	0.90
$T^*_{max,cell}$	0.80	0.95	0.87	0.75	0.67

Table 5
Performance evaluation of the optimally designed cell at C/2 discharge current.

Evaluation Index	Baseline Case	Optimization Cases			
		Case A	Case B	Case C	Case D
E^*_{cell}	1.18	1.33	1.30	1.22	1.07
$T^*_{max,cell}$	0.59	0.64	0.62	0.58	0.56

temperature of the optimally designed cell in case C are 5% higher and 6% lower compared to the baseline case, respectively. For this case, the thicknesses and porosities of both electrodes were decreased compared to the baseline design and the combined effects of these changes yield the cell with the specific energy and maximum temperature close to the corresponding values of the baseline case.

The performance of the optimally designed cell is evaluated under C/2 discharge current for all four cases. The results are summarized in Table 5. Similarly to the 1.5 C discharge scenario, both the specific energy and the maximum cell temperature are decreasing from case A (specific energy single objective) to case D (maximum temperature contributes 75% to the composite objective function). When operating at C/2 discharge current, the optimally designed cell delivers higher amount of energy at lower temperatures compared to 1.5 C discharge current. The maximum change in the delivered specific energy among the optimization cases with reference to the baseline case is circa 23% for both 1.5 C and C/2 discharge currents. However, the variation in the maximum cell temperature is 13.6% and 35% for C/2 and 1.5 C discharge currents, respectively. These results show that the impact of the cell design on the maximum cell temperature is further amplified under higher discharge currents.

Fig. 5 graphically illustrates the variations in the dimensionless cell voltage and temperature with the normalized discharge capacity for the baseline scenario and the optimization cases. As seen in Fig. 5-(a) and 5-(c), increasing the electrodes' thicknesses leads to higher delivered discharged capacities due to the increased volume of the active material to store mobile Li-ions. However, increasing the active material content results in higher ohmic overpotential, causing the voltage to drop in the middle of the discharge curve. The voltage drop is more significant for the cases with higher discharge current (1.5C) (Fig. 5-(c)). The corresponding cell temperature profiles during discharge are shown in Fig. 5-(b) and 5-(d). It is seen that the rate of the temperature increase versus discharge capacity is greater for thicker cells with the increased internal resistance and it is being further amplified by increasing the discharge current. To summarize, when compared to the baseline cell design, cases A and B have higher specific energies but also experience higher maximum temperatures; case C results in slightly higher specific energy and slightly lower maximum temperature; case D shows lower specific energy while experiencing lower maximum temperature. Hence, when considering the trade-offs between the cell specific energy and the maximum temperature, cases A and D emerge as favorable scenarios, respectively.

3.2. Pack performance analysis

The performance of the cells are investigated at the pack level. Four different battery packs were generated based on the four optimally designed cells (A, B, C, and D) presented in the Subsection 3.1. Table 6 summarizes the pack performance assessment under 1.5 C and C/2 discharge currents for the baseline case and the newly designed packs. The results comprise the dimensionless specific energy (E^*) and the maximum dimensionless temperature (T^*_{max}) of the pack. The latter is obtained by normalization using the maximum cut-off temperature specified for the pack. For the baseline case and the pack optimization cases A and B operating under discharge current 1.5 C, the maximum temperature exceeds the cut-off temperature threshold (i.e. $T^*_{max} > 1$) before the lower cut-off voltage is reached. When the discharge process begins, the cells located next to the load terminals are loaded by higher currents than the ones placed further away from the load points. Therefore, the temperature increases faster for the heavily loaded cells than for the rest of the pack. Pack cases A and B can deliver 7.9% and 10.5% higher specific energies than the baseline case at the cost of exceeding the pack cut-off temperature by 19% and 12%, respectively. It is observed that the pack design B delivers slightly higher specific energy than the pack design A under 1.5 C discharge current. This result illustrates that although thicker electrodes provide higher capacity (cell A), the drop in terminal voltage resulting from uneven discharge currents in parallel branches leads to reduced specific energy. Thus, pack B shows slightly higher specific energy compared to pack A. The results obtained from C/2 discharge current show that the pack behavior is compatible with the behavior of the corresponding optimally designed cell operating individually. This finding highlights the importance of cell-to-cell variations within battery packs subjected to high operating currents.

Fig. 6 depicts the drawn specific energy from the pack under

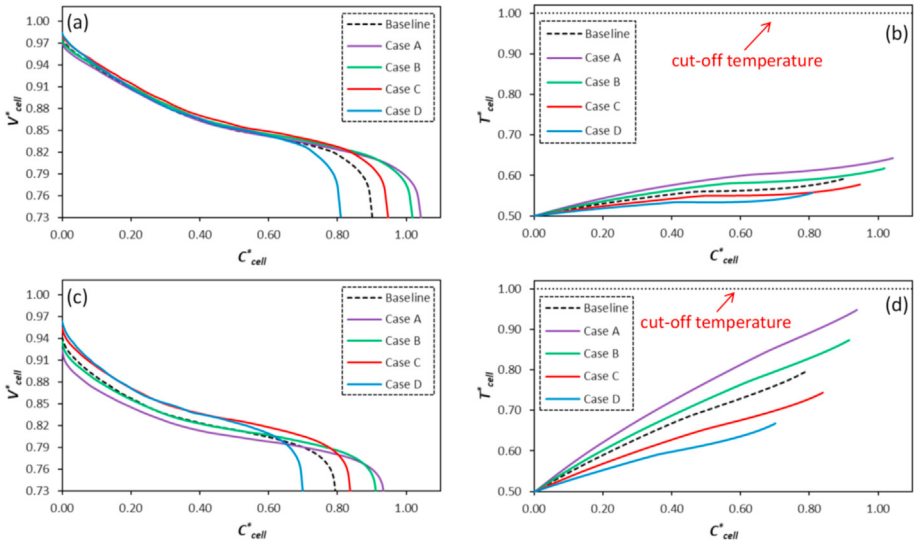

Fig. 5. Cell performance for the baseline and optimization cases. **(a):** Cell voltage at C/2 discharge. **(b):** Cell temperature at C/2 discharge. **(c):** Cell voltage at 1.5 C discharge. **(d):** Cell temperature at 1.5 C discharge.

Table 6
Battery pack performance evaluation at 1.5 C and C/2 discharge currents.

Discharge Current	Evaluation Index	Baseline Case	Optimization Cases			
			Case A	Case B	Case C	Case D
1.5 *C*	E^*_{pack}	0.38	0.41	0.42	0.38	0.32
	$T^*_{max,pack}$	1.01	1.19	1.12	0.93	0.80
C/2	E^*_{pack}	1.07	1.17	1.16	1.12	0.98
	$T^*_{max,pack}$	0.63	0.69	0.66	0.61	0.58

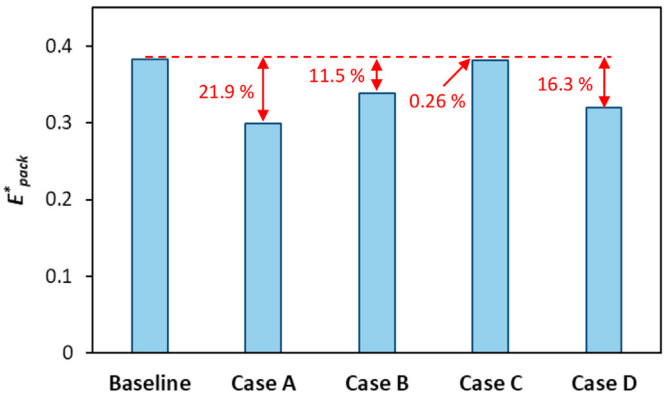

Fig. 6. Pack delivered specific energy under 1.5 C discharge up to the cut-off temperature limit.

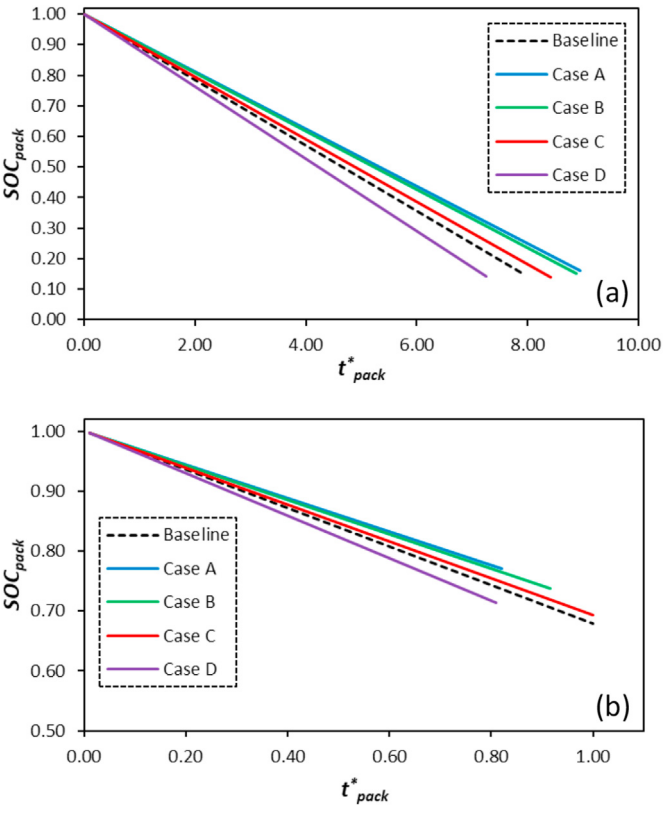

Fig. 7. State of charge profile of the pack under discharge process. **(a):** C/2 discharge operation. **(b):** 1.5 C discharge operation.

1.5C discharge while considering the pack cut-off temperature as the end of discharge criterion. Under this constraint, pack cases A and B deliver 21.9% and 11.5% lower specific energy than the baseline pack, respectively, due to the fast temperature rise of the thick cells with low porosities experiencing unequal discharge currents. Although pack case D does not undergo as rapid temperature rise as cases A and B, it provides 16.3% lower specific energy than the baseline design since it contains a smaller amount of active materials and hence delivers lower discharge capacities. Pack C delivers nearly the same specific energy as the base scenario but with 8% reduction in the pack maximum temperature (see Table 6).

Fig. 7 illustrates the SOC for all pack scenarios. As shown in Fig. 7-(a), under C/2 discharge operation, all cases deliver around 85% of the pack available capacity (i.e. $\Delta SOC = 0.85$). However, since cases A, B and C are made of remarkably less porous electrodes than the baseline scenario, they contain more active materials and hence can deliver higher capacities during the discharge process. Therefore, for the specific application under study, the battery pack discharge time is extended 12.6%, 11.7% and 6% by cases A, B and C, respectively in comparison with the baseline case. Pack D provides the lowest capacity among all cases with 8.7% reduction in its discharge time compared to the baseline scenario resulting in a reduced driving range. Fig. 7-(b) demonstrates that under 1.5 C discharge current, the discharge times of packs A and B are 17.9% and 8.3% shorter than the baseline case due to the rapid temperature rise of the constituting cells with high specific energies (see Table 6). Moreover, the operation of pack A that has highest capacity among all considered packs displays similar discharge time as case D with the lowest capacity, leaving 77% of the available capacity underutilized. Pack C on the other hand, shows nearly the same discharge profile as the baseline case both providing the most effective performances in terms of the battery pack energy utilization and discharge time under 1.5 C discharge current.

Fig. 8 depicts the average standard deviation of the temperature within the pack normalized with respect to the baseline case. It is observed that for discharge current 1.5 C, the normalized standard

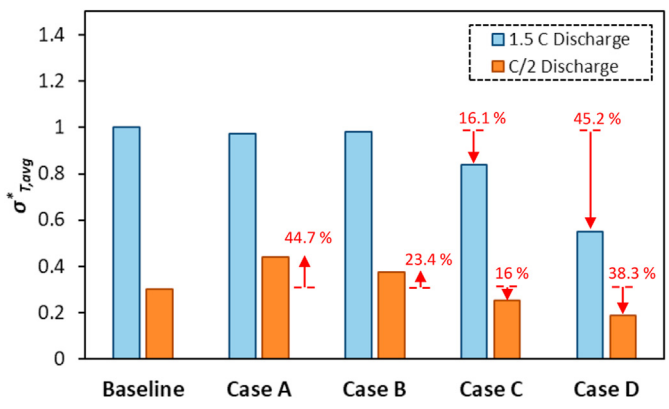

Fig. 8. Normalized average standard deviation of the temperature within the pack.

deviations $\sigma^*_{T,avg}$ are 2.2 (for pack A) to 3.3 (for the baseline pack) times higher compared to the corresponding values for C/2 discharge scenario. These results illustrate that the in-homogeneities in the module-to-module temperature profiles during the pack operation are more pronounced at a higher discharge current. When discharge current 1.5 C, packs A and B show approximately the same $\sigma^*_{T,avg}$ as the baseline pack up to the temperature cut-off limit. Packs C and D are displaying significantly improved thermal performance with 16.1% and 45.2% reduction in $\sigma^*_{T,avg}$, respectively, compared to the baseline scenario. For low discharge current C/2, pack A composed of the high-specific-energy cells experiences 44.7% increase in $\sigma^*_{T,avg}$, while pack D comprising the low-specific-energy cells results in 38.3% reduction in $\sigma^*_{T,avg}$ in comparison with the baseline case.

Fig. 9 visualizes module-to-module temperature variations for packs A, B, C and D. For the sake of simplicity, the temperature profiles are illustrated for three modules located in three different parallel branches (see Fig. 3): i) next to the load terminals (B_1), ii) far away from the load terminals (B_N) and, iii) one module in between (B_M). Fig. 9 correlates local temperatures within the pack to the time of discharge. It is seen that under low discharge current (C/2), none of the investigated packs cross the temperature cut-off limit (i.e. $T^*_{pack} = 1$) and therefore high-specific-energy packs (packs A and B) are superior in terms of providing longer time of discharge and hence delivered energy. However, higher discharge current (1.5 C) amplifies module-to-module temperature variations for packs A and B which leads to the fast temperature rise for the module located next to the load terminal (B_1) and thus limits the pack available energy to be fully utilized. Under such condition, pack C shows the most efficient energy performance among all cases, as well as preferable thermal performance compared to packs A and B. Fig. 9(e–h) illustrate that module B_1 experiences a descending trend in temperature profiles from $t^*_{pack} \approx 6$ when the packs are loaded by C/2 current. In fact, cell resistance increases as the SOC reduces most notably when the voltage approaches its lower cut-off threshold. Therefore, the modules close to the load terminals which initially experience higher currents, reach to the high impedance region earlier than the modules located further from the terminals. At this stage, the high cell internal resistance compensates for the low interconnection resistance and the current flow is reversed (i.e. modules further from the load terminals receive higher currents). When the cycling current is low (e.g. C/2),

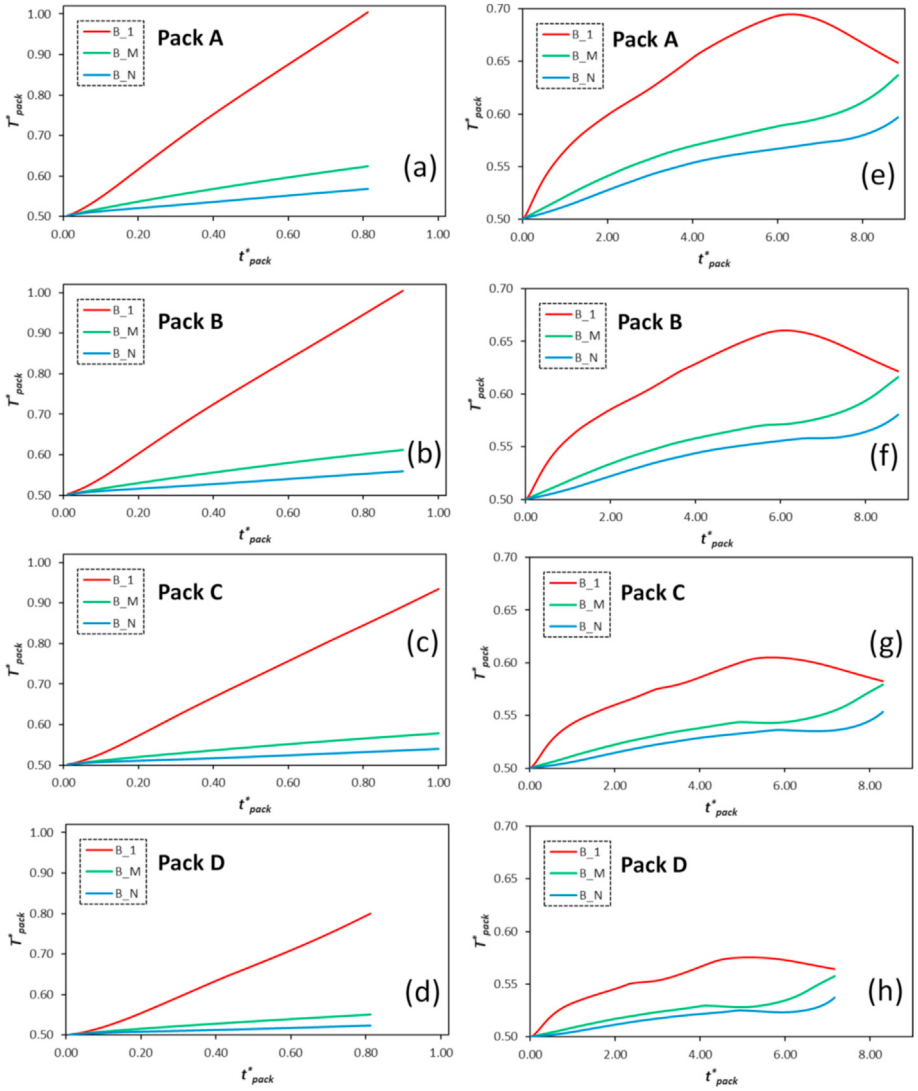

Fig. 9. Module-to-module temperature variations within the pack. **(a–d):** 1.5 C discharge operation. **(e–h):** C/2 discharge operation.

the modules face with the afore-stated phenomenon since the time of discharge is long enough and is not restricted by the fast temperature rise (i.e. cells/modules reach low SOC levels). At sufficiently low currents, the reversible heat (the second term on the right hand side in Equation 11) is comparable to the irreversible heat (the first term on the right hand side in Equation 11) and decreases the share of the heat generation rate compared to the heat dissipation rate in the energy conservation balance (see Equation 10) and in turn results in the above-mentioned temperature reduction trend.

3.3. Systematic analysis

Fig. 10 presents the Pareto front for designing the cell sandwich (optimized at 1.5 C discharge current and evaluated under C/2 discharge current) together with the corresponding curves showing the battery pack performance. The blue squares illustrate the optimal cell design alternatives and visualize the trade-offs between the considered objective functions (e.g. the specific energy and the maximum temperature). The interactions between the cell and the pack levels have not been reflected in these results and it can be assumed that the pack performance can be captured by only scaling up the cell model through the so-called lumped modeling technique. This approach is typically employed in already existing cell design optimization studies. Importantly, the present study leverages on the novel simulation optimization framework for identifying optimal cell design that considers cell-to-pack, represented by green circles in Fig. 10.

It is observed that for all cases and for both discharge currents (1.5 C and C/2), the pack shows lower amounts of the drawn specific energies and higher maximum temperatures in comparison with the corresponding values for the individual cell. The degree of deviation in the cell and pack performances is further amplified by increasing the discharge current. For instance, the battery pack operation for the baseline case under 1.5 C discharge current shows 61.7% lower specific energy and 26.3% higher maximum temperature compared to the cell. However, the corresponding values for C/2 discharge current are significantly lower, corresponding to 9.5% and 5.8% for the reduction in the specific energy and the increase in the maximum temperature, respectively. The inconsistency in the performances of the individual battery cells and the corresponding battery packs originates from the module-to-module extrinsic variations and imbalanced current distribution within the pack and therefore the cell behavior cannot be scaled up to the same pack performance. Fig. 10-(a) illustrates that under C/2 discharge current, neither the cells nor the packs reach the cut-off temperature limit. Furthermore, it is seen that with the increase in specific energy, there is an increase in the maximum temperature as well for all considered cell cases and for battery packs operating under C/2 discharge current. When packs A and B are operating under higher discharge current 1.5 C, pack B experiences slightly higher specific energy and lower maximum temperature, most likely due to uneven current distribution among the cells. Fig. 10-(b) clearly illustrates that although the individual cell operates below the cut-off temperature threshold for all design cases, pack designs A and B (along with the baseline pack case) experience higher temperatures than the cut-off value before the lower cut-off voltage limit is reached. Hence, packs A and B can potentially deliver higher specific energies than the baseline case only at the cost of crossing the cut-off temperature limit by 18.8% and 11.7%, respectively. Furthermore, when operating under 1.5 C discharge current packs A and B demonstrate the opposite behavior compared to the corresponding cells. Eventhough cell A has higher specific energy than cell B because of the higher cell thickness, the resulting potential drop due to the higher internal resistance of the thicker cell overcomes the capacity gain when operating in the pack. Hence, pack A is less thermally and energy efficient compared to pack B. Moreover, Fig. 10-(b) shows that pack C is equally energy efficient as the baseline case while experiencing 8% lower maximum temperature.

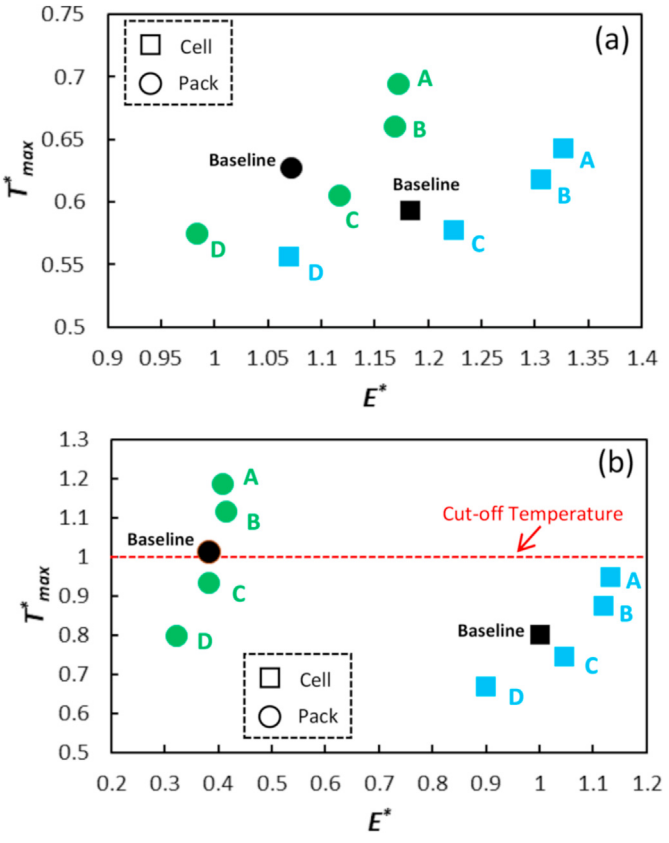

Fig. 10. Dimensionless cell/pack maximum temperature against specific energy. **(a):** C/2 discharge operation. **(b):** 1.5 C discharge operation.

The systemic analysis of the results reveals that if the model is not conscious of the cell-to-pack interactions, pack A yields to the maximum specific energy among all investigated designs without exceeding the cut-off temperature limit of the pack. However, when operating at 1.5 C current, the results show that some of the cell design alternatives (design cases A and B) are not favorable as they experience substantial temperature rise under pack working environment and therefore the pack available energy is underutilized. The integrated model in this research identifies pack C as the most favorable design (the highest specific energy together with thermally efficient performance of all studied cases) while considering cell-to-pack interactions. Fig. 10 brings forth a systematic decision support tool for cell manufacturers by providing a comprehensive overview already at the initial cell design stage about how various cell designs will affect the ultimate pack performance.

4. Conclusions

A comprehensive approach was developed in this research to evaluate the performance of the optimally designed Li-ion cells operating under battery pack working environment. The P2D electrochemical-thermally coupled model was employed for the cells using GT-AutoLion software in combination with the multi-objective optimization using NSGA-III-based genetic algorithm in GT-SUITE. The cathode and anode thicknesses and porosities were

selected as the design variables. Composite objective functions were considered with different weight factors (0, 0.25, 0.5, 0.75, and 1) being assigned to the specific energy and the maximum temperature of the cells. By varying contribution weights for the specific energy and the maximum cell temperature, respectively, four optimization cases were defined for the battery cell design: A (1, 0), B (0.75, 0.25), C (0.5, 0.5) and D (0.25, 0.75). The optimally designed cells were subsequently employed to construct four battery packs each comprising only one optimized cell type (referred to as pack A, B, C and D, respectively) to consider module-to-module operational variations due to current unbalance within the pack. The specific energy and the SOC for the battery packs were quantified to assess their energy utilization performance. Moreover, the maximum temperature and the average standard deviation of the temperature values within the pack were computed to evaluate the thermal performance of the packs. The cell design optimizations were performed under 1.5 C discharge current and the performance evaluation of the optimally designed cells was under C/2 discharge current. Results showed that considering the thermal efficiency at the cell design stage is essential for constructing battery packs with high specific energy and improved thermal performance especially under high rate cycling scenarios. It was observed that at 1.5 C discharge and when the cell-to-pack interactions are not considered (i.e. the cell performance can be scaled up to replicate the pack behavior), case A showed the highest achievable specific energy among all cases. However, the integrated model developed in this research suggests the pack comprising the optimally designed cells in which the specific energy and the maximum temperature were given the same weight (case C) as the most favorable design yielding the highest delivered specific energy compared to packs A, B and D. Furthermore, when operating at 1.5 C discharge current, pack C showed enhanced thermal performance compared to the baseline design with 8% reduction in the maximum pack temperature and 16.1% reduction in the average standard deviations of the temperature within the pack (i.e. improved module-to-module temperature variations).

The outcomes of this research expand the battery manufacturer's and designer's understanding in fabricating cells with improved energy and thermal performances to be efficiently integrated into large traction battery packs. Despite the fact that this study was mainly concentrated on the specific application of electric mining vehicles, the proposed framework is sufficiently robust and is applicable to other Li-ion battery powered energy systems with specific desired currents and load requirements. Moreover, to further enhance the model predictability, integrating the thermal circuit domain with the developed pack model will make the study even more suitable for real-world applications.

Funding

This work has been financially supported by the Swedish Energy Agency (project number P47906-1).

CRediT authorship contribution statement

Majid Astaneh: Conceptualization of this study, Methodology, Simulations, Writing - Original draft preparation. **Jelena Andric:** Conceptualization of this study, Methodology, Writing - review and editing. **Lennart Löfdahl:** Overall guidance. **Peter Stopp:** Software consultancy.

Declaration of competing interest

The authors declare that they have no known competing financial interests or personal relationships that could have appeared to influence the work reported in this paper.

Acknowledgement

The computations were enabled by resources provided by the Swedish National Infrastructure for Computing (SNIC) at Tetralith (NSC) [50].

Nomenclature

List of Symbols

A	cell surface area (m^2)
a_s	interfacial surface area (m^{-1})
a/c	anode-to-cathode capacity ratio
C	capacity (Ah)
c	lithium concentration ($mol.m^{-3}$)
c_p	specific heat ($J.kg^{-1}.K^{-1}$)
D	diffusion coefficient ($m^2.s^{-1}$)
E	specific energy ($Wh.kg^{-1}$)
F_{cell}	composite objective function
F	Faraday's constant ($C.mol^{-1}$)
h	heat transfer coefficient ($W.m^{-2}.K^{-1}$)
I	current (A)
i	design factor number
i_0	exchange current density ($A.m^{-2}$)
j^{Li}	intercalation current density ($A.m^{-3}$)
k	ionic conductivity ($S.m^{-1}$)
L	thickness (μm)
M	mass (kg)
N	number of modules connected in parallel
n	number of cells
Q_{gen}	generated heat (W)
R	universal gas constant ($J.(mol.K)^{-1}$)
r	radial coordinate
T	temperature (°C)
t	time (s)
t_0^+	transference number
U	open circuit voltage (V)
V	voltage (V)
w	wight factor
x	spatial coordinate
x_i	design factors
$x_{0\%,100\%}$	stoichiometry factors of the anode at 0% and 100% SOC
$y_{0\%,100\%}$	stoichiometry factors of the cathode at 0% and 100% SOC

Greek Letters

α	charge transfer coefficient
ϵ	volume fraction or porosity
η	overpotential (V)
μ	mean value
ρ	density ($kg.m^3$)
σ^{eff}	effective electronic conductivity ($S.m^{-1}$)
σ_T	standard deviation of temperature
φ	electric potential (V)
ψ	transport property (D_e and k)

Subscripts/ Superscripts

an	anode
b	baseline
c	charge
ca	cathode
$cell$	battery cell
e	electrolyte

eff	effective
d	discharge
E	specific energy
f	filler
j	module number
pa	parallel
pack	battery pack
s	solid
se	series
sep	separator
T	temperature
*	dimensionless value

Abbreviations

amb	ambient
avg	Average
BEV	battery electric vehicle
EV	electric vehicle
LFP	lithium iron phosphate
Li-ion	lithium-ion
max	Maximum
NCA	lithium nickel cobalt aluminum oxide
NMC	lithium nickel manganese cobalt oxide
nom	nominal
NSGA	non-dominated sorting genetic algorithm
PHEV	plug-in hybrid electric vehicle
P2D	pseudo-two dimensional
SOC	state of charge

References

[1] Ghorbanzadeh M, Astaneh M, Golzar F. Long-term degradation based analysis for lithium-ion batteries in off-grid wind-battery renewable energy systems. Energy 2019;166:1194–206.

[2] Gao Y, Zhu C, Zhang X, Guo B. Implementation and evaluation of a practical electrochemical- thermal model of lithium-ion batteries for EV battery management system. Energy 2021;221:119688.

[3] Goodenough JB. Electrochemical energy storage in a sustainable modern society. Energy Environ Sci 2014;7(1):14–8.

[4] Zhong Z, Chen L, Huang S, Shang W, Kong L, Sun M, et al. Single-crystal LiNi0.5Co0.2Mn0.3O2: a high thermal and cycling stable cathodes for lithium-ion batteries. J Mater Sci 2019;55:2913–22.

[5] Sim S-J, Lee S-H, Jin B-S, Kim H-S. Use of carbon coating on LiNi0.8-Co0.1Mn0.1O2 cathode material for enhanced performances of lithium-ion batteries. Sci Rep 2020;10(1):11114.

[6] Vlad A, Singh N, Galande C, Ajayan PM. Design considerations for unconventional electrochemical energy storage architectures. Adv Energy Mater 2015;5(19):1402115.

[7] Campbell ID, Gopalakrishnan K, Marinescu M, Torchio M, Offer GJ, Raimondo D. Optimising lithium-ion cell design for plug-in hybrid and battery electric vehicles. J Energy storage 2019;22:228–38.

[8] Xue N, Du W, Gupta A, Shyy W, Marie Sastry A, Martins JRRA. Optimization of a single lithium-ion battery cell with a gradient-based algorithm. J Electrochem Soc 2013;160(8). A1071–A1078.

[9] Lu W, Jansen A, Dees D, Nelson P, Veselka NR, Henriksen G. High-energy electrode investigation for plug-in hybrid electric vehicles. J Power Sources 2011;196(3):1537–40.

[10] De S, Northrop PWC, Ramadesigan V, Subramanian VR. Model-based simultaneous optimization of multiple design parameters for lithium-ion batteries for maximization of energy density. J Power Sources 2013;227:161–70.

[11] Hosseinzadeh E, Marco J, Jennings P. Electrochemical-thermal modelling and optimisation of lithium-ion battery design parameters using analysis of variance. Energies 2017;10(9):1278.

[12] Appiah WA, Park J, Song S, Byun S, Ryou M-H, Lee YM. Design optimization of LiNi0.6Co0.2Mn0.2O2/graphite lithium-ion cells based on simulation and experimental data. J Power Sources 2016;319:147–58.

[13] Xu M, Reichman B, Wang X. Modeling the effect of electrode thickness on the performance of lithium-ion batteries with experimental validation. Energy 2019;186:115864.

[14] Becker MC, Salvatore P, Zirpoli F. The impact of virtual simulation tools on problem-solving and new product development organization. Res Pol 2005;34(9):1305–21.

[15] Doyle M, Fuller TF, Newman J. Modeling of galvanostatic charge and discharge of the lithium/polymer/insertion cell. J Electrochem Soc 1993;140(6):1526–33.

[16] Srinivasan V, Newman JS. Design and optimization of a natural graphite/iron phosphate lithium-ion cell. J Electrochem Soc 2004;151(10). A1530–A1538.

[17] Liang J, Gan Y, Tan M, Li Y. Multilayer electrochemical-thermal coupled modeling of unbalanced discharging in a serially connected lithium-ion battery module. Energy 2020;209:118429.

[18] Liu C, Liu L. Optimal design of Li-ion batteries through multi-physics modeling and multi-objective optimization. J Electrochem Soc 2017;164(11). E3254–E3264.

[19] Lee D-C, Lee K-J, Kim C-W. Optimization of a lithium-ion battery for maximization of energy density with design of experiments and micro-genetic algorithm. Int J Precis Eng Manuf Green Technol 2020;7(4):829–36.

[20] Elsewify O, Souri M, Esfahani MN, Hosseinzadeh E, Jabbari M. A new method for internal cooling of a large format lithium-ion battery pouch cell. Energy 2021;225:120139.

[21] Wu N, Ye X, Li J, Lin B, Zhou X, Yu B. Passive thermal management systems employing hydrogel for the large-format lithium-ion cell: a systematic study. Energy 2021;231:120946.

[22] Liu X, Ai W, Naylor Marlow M, Patel Y, Wu B. The effect of cell-to-cell variations and thermal gradients on the performance and degradation of lithium-ion battery packs. Appl Energy 2019;248:489–99.

[23] Mevawalla A, Panchal S, Tran M-K, Fowler M, Fraser R. Mathematical heat transfer modeling and experimental validation of lithium-ion battery considering: tab and surface temperature, separator, electrolyte resistance, anode-cathode irreversible and reversible heat. Batteries 2020;6(4):61.

[24] Mevawalla A, Panchal S, Tran M-K, Fowler M, Fraser R. One dimensional fast computational partial differential model for heat transfer in lithium-ion batteries. J Energy storage 2021;37:102471.

[25] Bruen T, Marco J. Modelling and experimental evaluation of parallel connected lithium ion cells for an electric vehicle battery system. J Power Sources 2016;310:91–101.

[26] Hosseinzadeh E, Marco J, Jennings P. Combined electrical and electrochemical-thermal model of parallel connected large format pouch cells. J Energy storage 2019;22:194–207.

[27] Hosseinzadeh E, Arias S, Krishna M, Worwood D, Barai A, Widanalage D, et al. Quantifying cell-to-cell variations of a parallel battery module for different pack configurations. Appl Energy 2021;282:115859.

[28] Newman J, Thomas KE, Hafezi H, Wheeler DR. Modeling of lithium-ion batteries. J Power Sources 2003;119–121:838–43.

[29] Ramadesigan V, Northrop PWC, De S, Santhanagopalan S, Braatz RD, Subramanian VR. Modeling and simulation of lithium-ion batteries from a systems engineering perspective. J Electrochem Soc 2012;159(3):R31–45.

[30] Brand MJ, Hofmann MH, Steinhardt M, Schuster SF, Jossen A. Current distribution within parallel-connected battery cells. J Power Sources 2016;334:202–12.

[31] Astaneh M, Andric J, Löfdahl L, Maggiolo D, Stopp P, Moghaddam M, et al. Calibration optimization methodology for lithium-ion battery pack model for electric vehicles in mining applications. Energies 2020;13(14):3532.

[32] Liang J, Gan Y, Li Y, Tan M, Wang J. Thermal and electrochemical performance of a serially connected battery module using a heat pipe-based thermal management system under different coolant temperatures. Energy 2019;189:116233.

[33] Cordoba-Arenas A, Onori S, Rizzoni G. A control-oriented lithium-ion battery pack model for plug-in hybrid electric vehicle cycle-life studies and system design with consideration of health management. J Power Sources 2015;279:791–808.

[34] Huang D, Chen Z, Zheng C, Li H. A model-based state-of-charge estimation method for series-connected lithium-ion battery pack considering fast-varying cell temperature. Energy 2019;185:847–61.

[35] Gamma Technologies. GT-SUITE user manual, version 2020 build 1.0001. Westmont, IL, USA: Gamma Technologies; 2020.

[36] Prada E, Di Domenico D, Creff Y, Bernard J, Sauvant-Moynot V, Huet F. Simplified electrochemical and thermal model of LiFePO4-graphite Li-ion batteries for fast charge applications. J Electrochem Soc 2012;159(9). A1508–A1519.

[37] https://northvolt.com/.
[38] Golmon S, Maute K, Dunn ML. A design optimization methodology for Li+ batteries. J Power Sources 2014;253:239–50.
[39] Thorat IV, Joshi T, Zaghib K, Harb JN, Wheeler DR. Understanding rate-limiting mechanisms in LiFePO4 cathodes for Li-ion batteries. J Electrochem Soc 2011;158(11):A1185–93.
[40] Du W, Gupta A, Zhang X, Sastry AM, Shyy W. Effect of cycling rate, particle size and transport properties on lithium-ion cathode performance. Int J Heat Mass Tran 2010;53(17):3552–61.
[41] Zhang L, Wang L, Hinds G, Lyu C, Zheng J, Li J. Multi-objective optimization of lithium-ion battery model using genetic algorithm approach. J Power Sources 2014;270:367–78.
[42] Gong X, Xiong R, Mi CC. Study of the characteristics of battery packs in electric vehicles with parallel-connected lithium-ion battery cells. In: 2014 IEEE Applied Power Electronics Conference and Exposition - APEC 2014; 2014. p. 3218–24.
[43] Offer GJ, Yufit V, Howey DA, Wu B, Brandon NP. Module design and fault diagnosis in electric vehicle batteries. J Power Sources 2012;206:383–92.
[44] Neupert S, Kowal J. Inhomogeneities in battery packs. World Electr Veh J 2018;9(2):20.
[45] Zahid T, Xu K, Li W, Li C, Li H. State of charge estimation for electric vehicle power battery using advanced machine learning algorithm under diversified drive cycles. Energy 2018;162:871–82.
[46] Bi J, Wang Y, Zhang J. A data-based model for driving distance estimation of battery electric logistics vehicles. EURASIP J Wireless Commun Netw 2018;2018(1):251.
[47] Rumpf K, Naumann M, Jossen A. Experimental investigation of parametric cell-to-cell variation and correlation based on 1100 commercial lithium-ion cells. J Energy storage 2017;14:224–43.
[48] Basu S, Hariharan KS, Kolake SM, Song T, Sohn DK, Yeo T. Coupled electrochemical thermal modelling of a novel Li-ion battery pack thermal management system. Appl Energy 2016;181:1–13.
[49] Choi H, Lim N-g, Lee SJ, Park J. Feasibility study for sustainable use of lithium-ion batteries considering different positive electrode active materials under various driving cycles by using cell to electric vehicle (EV) simulation. Sustainability 2020;12(22):9764.
[50] SNIC. Swedish national infrastructure for computing. 2020 [URL https://www.snic.se/].